ıl Analysis of Metal-Foam Application for Trailing Edge Noise Reduction

Christopher Teruna [*], Farhan Manegar [†], Francesco Avallone [‡], Damiano Casalino [§], Daniele Ragni [¶], Alejandro Rubio-Carpio [ǁ], Thomas Carolus [**]

This manuscript presents a numerical investigation of the turbulent boundary layer-trailing edge (TBL-TE) noise reduction with an open-cell porous material. The implementation of the porous media is verified by emulating a facility for characterizing the flow resistivity of the porous material. Subsequently, the porous media is applied on the trailing edge of a NACA 0018 airfoil to examine its capability to mitigate TBL-TE noise. The airfoil is set at zero angle of attack and the chord-based Reynolds number is 2.8×10^5. Boundary layer profiles and integral boundary layer quantities have been compared with reference experimental data. The noise reduction obtained with the porous trailing edge at low to mid frequency ranges has been found to be in good agreement with the experiment. However, the simulation is unable to predict the noise increase at high frequency, which is considered due to the neglected surface roughness effects in the adopted porous media model. Conventional beamforming is also used to locate the dominant sound sources. In contrast with the solid trailing edge case, it has been found that the solid-porous interface is the location of the dominant sound source for the porous trailing edge case.

I. Nomenclature

C	=	form coefficient (m^{-1})
C_p	=	pressure coefficient
c	=	chord length (m)
d_c	=	mean porous cell diameter (μm)
K	=	permeability (m^2)
H	=	shape factor
h	=	porous media thickness (mm)
p'	=	pressure fluctuation (Pa)
R_I	=	inertial resistivity (m^2)
R_V	=	viscous resistivity (Ns/m^4)
$SPL_{1/3}$	=	sound pressure level in third octave bands (dB)
u	=	wall-parallel velocity fluctuation component (m/s)
v	=	wall-normal velocity fluctuation component (m/s)
U_∞	=	mean freestream velocity (m/s)
v_d	=	darcian velocity (m/s)
ΔP	=	pressure drop across porous media (Pa)
δ^*	=	displacement thickness (mm)
δ_{99}	=	boundary layer thickness at 99 % U_∞ (mm)
Φ	=	power spectral density (dB/Hz)
ϕ	=	porosity (%)
θ_*	=	momentum thickness (mm)

[*]Doctoral candidate, Wind Energy Department, Delft University of Technology, Delft 2629HS, The Netherlands. AIAA Student Member.

[†]Doctoral candidate, Institute for Fluid and Thermodynamics, University of Siegen, Siegen, 57076, Germany, AIAA Student Member

[‡]Assistant professor, Wind Energy Department, Delft University of Technology, Delft 2629HS, The Netherlands. AIAA Member.

[§]Professor, Wind Energy Department, Delft University of Technology, Delft 2629HS, The Netherlands. AIAA Member.

[¶]Assistant professor, Delft University of Technology, Delft 2629HS, The Netherlands. Wind Energy Department, AIAA Member.

[ǁ]Doctoral candidate, Wind Energy Department, Delft University of Technology, Delft 2629HS, The Netherlands. AIAA Student Member.

[**]Professor, Institute for Fluid and Thermodynamics, University of Siegen, Siegen, 57076, Germany, AIAA Member

II. Introduction

AIRFOIL self-noise is one of the most prevalent noise sources in both aeronautics [1] and wind energy [2] industries. Since high Reynolds number flow is quite common in these applications, the turbulent boundary layer-trailing edge (TBL-TE) noise [3, 4] often serves as the primary sound generation mechanism, which subsequently leads to the investigations of various noise mitigation techniques in the literature, such as the trailing edge serrations [2, 5, 6], and the open-cell porous materials [7–10]. As suggested by the name, open-cell porous materials have interconnected pores that allow fluid to permeate through. For the sake of brevity, however, the open-cell porous materials will be referred simply as "porous materials" for the rest of this manuscript.

Sarradj and Geyer [11] studied the effects of different types of porous materials on the aerodynamics and acoustics response of a SD7003 airfoil. The porous materials were characterized using two parameters, namely the flow resistivity and the porosity. While no clear relationship between the material parameters and the acoustics response of the airfoil was found, the porous airfoils were observed to be quieter yet with lower aerodynamic performance. The same authors extended the study [9] by limiting the airfoil permeability at the aft section of the airfoil. This was achieved by covering the upstream portion of the porous airfoil with a non-permeable foil, which allows the streamwise extent of the porous trailing edge to be adjusted. They found that the more portion of the porous surface is exposed, the larger the noise reduction is when compared to the corresponding solid airfoil.

A more recent study about the application of porous material to reduce trailing edge noise has been performed by Rubio-Carpio et al. [10]. They performed acoustic beamforming and PIV measurements on a NACA 0018 airfoil whose trailing edge was replaceable with a metal-foam insert. Various porosity and resistivity values were examined using metal-foam of different pore sizes. The aerodynamics of the airfoil was studied and the pressure distribution upstream of the solid-porous interface was reported to be unchanged when the metal-foam insert was installed. This suggested that the changes in the airfoil loading distribution was isolated at the porous trailing edge region. Noise reduction was achieved at lower to medium frequency ranges, although there was a noticeable noise increase at high frequency. The noise increase was attributed to the increased surface roughness of the metal-foam [12]. In a follow-up study [13], the authors performed additional tests to determine the role of permeability of the material on the noise reduction. In addition to the trailing edge inserts from the previous study, a "non-permeable" metal-foam trailing edge was manufactured by adding a layer of adhesive at the symmetry plane of the metal-foam insert. This treatment prevented cross-flow through the porous material from taking place. Interestingly, they observed that the non-permeable trailing edge did not cause noise reduction at lower to medium frequency ranges, while the noise increase in the high frequency remained. Thus, the noise reduction mechanism of the porous trailing edge was considered to be related with the unsteady flow across the metal-foam. Nonetheless, they warranted further analyses as there were still insufficient information to reach a conclusion on how the unsteady cross-flow could cause noise reduction. A high fidelity numerical simulation might be a viable option to complement the experimental results in order to better understand the involved physical mechanisms.

Numerical studies on the aeroacoustics applications of porous materials have been reported in the literature. For instance, Liu et al. investigated the effect of porous material coating on a cylinder [14] and a tandem cylinder [15] configurations. The porous coating was represented as an equivalent fluid region where the mass and momentum conservation equations were modified to include Brinkman-Forchheimer-Darcy model (sometimes also referred as the Hazen-Dupuit-Darcy model [16]). The velocity terms in the momentum equation were replaced with Darcian velocity (average mass flow inside a porous material) and additional terms associated with the porous media resistivity were added. This strategy was preferred over considering the detailed internal topology of the porous material, since the latter may be prohibitively expensive without necessarily adding useful details to the results [17]. For both the isolated cylinder and the tandem cylinder configurations, the authors have shown that the porous coating reduced the intensity of the vortex shedding tone. Furthermore, by varying the thickness of the porous coating, the vortex shedding process of the cylinders could be suppressed. Nonetheless, their study suggested that the Darcy's law would be suitable to emulate the characteristics of porous materials in numerical simulations.

The goal in this manuscript is to verify and validate the numerical implementation of the porous media model based on the Darcy's law in the context of TBL-TE noise reduction. Firstly, the porous media model is verified using a porous material characterization rig [10]. This setup examines the consistency of the porous media model in resolving the pressure drop across a porous material sample. Subsequently, the porous media model is applied for the case of a NACA 0018 equipped with a metal-foam trailing edge [13] to determine whether the aeroacoustics response of the porous trailing edge (e.g., noise reduction) could be replicated by the simulation. The study will be extended to further elucidate the noise reduction mechanism of the porous trailing edge and other potential applications of porous materials,

such as for reducing the turbulence impingement noise.

The manuscript is organized as follows. Section III provides a brief description on the porous material characterization and the following methodologies, including the metal-foam trailing edge setup and an overview of Lattice-Boltzmann method in PowerFLOW. Section IV discusses the simulation results, which is summarized afterward in Section V.

III. Methodologies

A. Describing the Macroscopic Transport Phenomena in Porous Materials

Up to 6 different parameters can be used to characterize the macroscopic properties of transport phenomena in porous materials [16], although the most common ones in literature are porosity, permeability, and form coefficient [10, 11, 15]. The porosity of the material is defined as:

$$\phi = 1 - \frac{\rho_p}{\rho_s} \tag{1}$$

where ρ_p and ρ_s are density of the porous material sample and that of the solid (non-permeable) sample, respectively. Meanwhile, the permeability and the form coefficient can be obtained through the Hazen-Dupuit-Darcy equation [16]. This equation describes the pressure loss Δp when a certain mass flow permeates through a porous material sample of thickness h, as follows.

$$\frac{\Delta p}{h} = \frac{\mu_\infty}{K} v_d + \rho_\infty C v_d^2 \tag{2}$$

where μ_∞ and ρ_∞ is the fluid's freestream dynamic viscosity and density respectively, while K and C are the permeability and the form coefficient of the porous material. Equation 2 is valid for porous materials whose pore size is much smaller than the characteristic length (e.g., thickness) of the sample.

The Hazen-Dupuit-Darcy equation forms a second order polynomial in term of Darcian velocity v_d which equals to the ratio of the mass flow through the sample against the sample's cross section area. The linear term of the equation describes the contribution of viscous loss within the porous material, and thus the coefficient μ_∞/K is also referred to as the viscous resistivity R_V. Meanwhile the second term describes the inertial resistance due to local flow acceleration within the pores, which links the form coefficient C to the inertial resistivity R_I. Compared to the viscous resistivity, the inertial resistivity would only become significant when large mass flow rate is involved [16].

The porous material in this study is a metal-foam made of NiCrAl alloy manufactured by *Alantum*. The manufacturer classified the metal-foam samples using their mean cell diameter d_c; two types of the metal-foam (i.e., 450 μm and 800 μm) are investigated in this study. The characterization of the metal-foam was performed by Rubio-Carpio et al. [10] as reported in Table 1. They obtained R_V and R_I by curve-fitting a series of pressure drop tests with Eq. 2. Note that the values listed in Table 1 are asymptotic values for metal-foam samples, i.e., for a sample whose thickness is above a critical value [18]. The critical thickness was also reported to depend on the pore size on the metal-foam.

Table 1   Parameters for characterizing transport phenomena in the metal-foam samples

d_c (μm)	ϕ(%)	R_V (N s/m^4)	R_I (m^{-1})
450	89.28	29850	9758
800	91.65	6728	2613

B. Numerical Solver

This section provides a brief summary of the numerical technique implemented in the commercial Lattice-Boltzmann solver PowerFLOW 5.4b. For more details on the theoretical foundation of the Lattice-Boltzmann method (LBM), however, readers are advised to refer to Succi [19]. The LBM is based on Boltzmann's kinetic theory of gases which describes the microscopic behavior of fluid particles. This is mathematically expressed as follows;

$$\frac{\partial F}{\partial t} + V \cdot \nabla F = \mathbf{B} \tag{3}$$

where $F(\boldsymbol{x}, t)$ is the particle distribution function in spatial ($\boldsymbol{x}$) and temporal space (t), V is the particle velocity, and $\mathbf{B}$ is the collision operator. The equation is then discretized on a cartesian grid, referred to as a lattice, where the fluid motion is limited to a set of discrete dimensions and vectors. PowerFLOW employs the D3Q19 model for solving low Mach number cases [20–22]. The discretized form of the LBM is written as follows;

$$F_{\mathrm{n}}(\boldsymbol{x} + \boldsymbol{V}_{\mathrm{n}}\Delta t, t + \Delta t) - F_{\mathrm{n}}(\boldsymbol{x}, t) = \mathbf{B}_{\mathrm{n}}(\boldsymbol{x}, t) \tag{4}$$

where F_{n} is the particle distribution function in n^{th} direction in the lattice, $\boldsymbol{V}_{\mathrm{n}}$ is the discrete particle velocity in n^{th} direction. The collision term $\mathbf{B}_{\mathrm{n}}$ follows the Bhatnagar-Gross-Krook model [23];

$$\mathbf{B}_{\mathrm{n}} = -\frac{\Delta t}{\tau}[F_{\mathrm{n}}(\boldsymbol{x}, t) - F_{\mathrm{n}}^{\mathrm{eq}}(\boldsymbol{x}, t)] \tag{5}$$

where τ is the relaxation time which is a function of fluid viscosity and temperature, while $F_{\mathrm{n}}^{\mathrm{eq}}$ is the equilibrium distribution function can be approximated with a second-order expansion as follows [22];

$$F_{\mathrm{n}}^{\mathrm{eq}} = \rho\omega_{\mathrm{n}}\left[1 + \frac{\boldsymbol{V}_{\mathrm{n}}\boldsymbol{u}}{a_s^2} + \frac{(\boldsymbol{V}_{\mathrm{n}}\boldsymbol{u})^2}{2a_s^4} - \frac{|\boldsymbol{u}|^2}{2a_s^2}\right] \tag{6}$$

where ω_{n} are the weighting functions based on the D3Q19 model, and $a_s = \frac{1}{\sqrt{3}}$ is the non-dimensional speed of sound within the lattice.

Solving Eq. 4 for obtaining $F(\boldsymbol{x}, t)$ allows the recovery of macroscopic flow quantities, such as density ρ and velocity $\vec{u}$ which are mathematically expressed as follow;

$$\rho(\boldsymbol{x}, t) = \sum_{\mathrm{n}} F_{\mathrm{n}}(\boldsymbol{x}, t) \tag{7}$$

$$\rho\boldsymbol{u}(\boldsymbol{x}, t) = \sum_{\mathrm{n}} V_{\mathrm{n}} F_{\mathrm{n}}(\boldsymbol{x}, t) \tag{8}$$

The simulation domain has been discretized into cubic volumetric elements, also referred to *voxel* (i.e., volumetric pixel). The dimension of each voxel may be adjusted accordingly where detailed flow description is necessary (e.g., in the vicinity of a wall with arbitrary geometry). The domain is then subdivided into smaller regions in which voxel dimensions of adjacent region is allowed to vary by a factor of 2. A Very Large Eddy Simulation (VLES) model based on two-equations $k - \epsilon$ Renormalization Group (RNG) [24] has been adopted. A wall function is applied to the wall-adjacent grid, which is based on generalized law-of-the-wall model [25], extended by considering the effect of pressure gradient and surface roughness. For computing far-field noise, PowerFLOW employs Ffowcs-Williams & Hawking (FW-H) analogy [26] based on Farrasat's formulation 1A [27] with forward-time solution [28], extended for application on permeable integration surfaces.

C. Numerical Implementation of the Fluid Transport Across the Porous Media

There are two approaches for replicating the porous media * in a numerical simulation, 1) resolving the internal topology of the porous media, or 2) recovering the macroscopic fluid behavior inside the porous media with simplified models (e.g., Darcy's law). The latter is often more feasible to apply since the internal structure of the porous media is replaced with a boundary condition [29] or an equivalent fluid region [30] with additional properties to describe the flow field interaction with the porous media. Since this study adopts a porous media model to mimic the behavior of the

---

*i.e., a collective term for media with part of their internal volume being hollow, ranging from the micropores in a sponge to a mesh of heat exchanger tubes

metal-foam, this section briefly discusses the implementation of the Darcian law in PowerFLOW. For more details, readers are advised to refer to Freed [17] and Sun et al. [30].

A porous media can be treated as a region of momentum sink as described by the Darcy's law, which states that the pressure gradient ∇p for a flow permeating through a porous material is proportional to the local flow velocity $\boldsymbol{u}$, as follows;

$$\nabla p = -\boldsymbol{R} \cdot \boldsymbol{u} \tag{9}$$

where $\boldsymbol{R}$ is the total resistivity which represents the sum of the viscous and inertial resistivity components ($\boldsymbol{R}_V$ and $\boldsymbol{R}_I$ respectively). Eq. 9 is also referred to as Darcy's force equation. $\boldsymbol{R}$ can be expanded as in Eq. 10. Comparing the resulting equation to the Hazen-Dupuit-Darcy equation (Eq. 2) would reveal the following relationship between permeability and form coefficient with the viscous and inertial resistivity respectively.

$$\boldsymbol{R} = \boldsymbol{R}_V + \boldsymbol{R}_I \boldsymbol{u} \; ; \qquad \boldsymbol{R}_V = \frac{\mu_\infty}{\rho_\infty \boldsymbol{K}} \; , \; \boldsymbol{R}_I = \boldsymbol{C} \tag{10}$$

It has been shown that the LBM is equivalent to Navier-Stokes equations using Chapman-Enskog expansion up to third-order truncation for perfect gas at low Mach number [22]. Hence, Eq. 9 can be substituted to Eq. 4, and the resulting equation would be equivalent to the following Navier-Stokes form;

$$\frac{\partial \rho}{\partial t} + \nabla \cdot (\rho \boldsymbol{u}) = 0 \tag{11}$$

$$\frac{\partial \rho \boldsymbol{u}}{\partial t} + \nabla \cdot (\rho \boldsymbol{u} \boldsymbol{u}) = -\nabla p - \boldsymbol{R} \cdot \boldsymbol{u} \tag{12}$$

where the regular viscous term in Eq. 12 has been replaced by the Darcy's force which accounts for both the viscous drag caused by the topology of the porous material, as well as additional inertial resistance when the local Reynolds number is sufficiently high. For the interface between the regular fluid region and the porous media region, double-sided surfaces are applied similar to sliding mesh [30]. Moreover, to satisfy mass-flux conservation at the interface, the following expression is adopted;

$$|\rho u_n|_\infty = \phi |\rho u_n|_{\text{PM}} \tag{13}$$

where ϕ is the material porosity, while the subscripts ∞ and PM denote the regular fluid region and porous media region respectively.

There are, however, two models of porous media in PowerFLOW, (1) APM (acoustics porous medium) and (2) PM (porous medium) with small differences. While both describes the porous material as an equivalent fluid region where the Darcian forces apply, the APM also considers the acoustic absorption property of the material. In this regard, the interface of the APM region can be specified with a porosity, which in turn governs the the mass flow between the regular fluid region and the APM region. It has been shown in the literature [30] that using empirical resistivity and porosity values would usually be sufficient for rigid porous materials, although for others (e.g., felt or polymer foam), the parameters may require slight adjustments [31] to achieve more accurate aerodynamic and acoustic response. Moreover, PowerFLOW's PM-APM models do not consider various porous material properties, such as surface roughness, thermal dissipation, and elasticity. In particular, surface roughness effects have been observed to have relevant contribution toward additional noise at high frequency ranges for the porous trailing edge case [9, 13]. Thus, this aspect of the experiment is expected to not be replicated in the simulation.

IV. Computational Setup

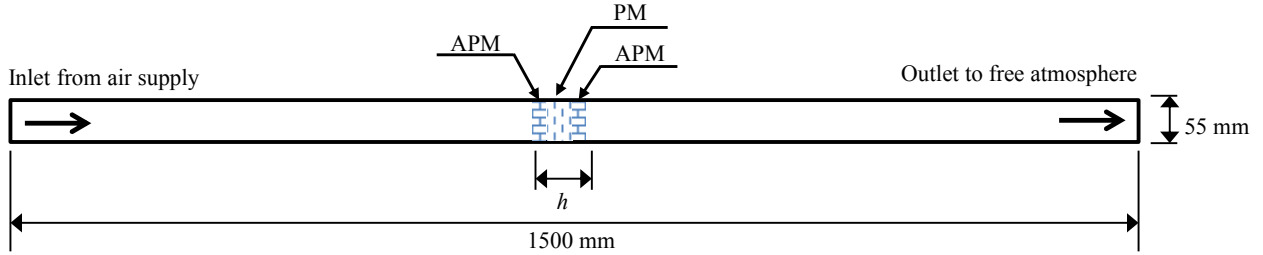## A. Porous Material Characterization Test Rig

Fig. 1   Simplified sketch of the test rig for characterizing the permeability and the form coefficient of the metal-foam sample.

The purpose of this experimental test rig is to obtain the permeability and form coefficient (i.e., viscous and inertial resistivity respectively) of a metal-foam sample by measuring the pressure drop across the sample. The main component of the test rig is a straight tube with one end exposed to the ambient pressure and the other to an air reservoir. This reservoir can be controlled to impose a certain mass flow at the inlet of the tube, and consequently the Darcian velocity across the metal-foam sample. The tube itself is 1.5 m long with a circular cross section of 55 mm in diameter, in which the metal-foam sample is contained within an adapter that is inserted into the middle section of the tube. Various sample thickness (h) can be tested by choosing a suitable adapter. The pressure drop (Δp) measurements are performed using pressure taps located at 50 mm upstream and downstream of the sample. Subsequently, the permeability and form coefficient of the sample is obtained by curve fitting the pressure drop trend across a range of Darcian velocity with the Hazen-Dupuit-Darcy equation (Eq. 2). A simplified sketch of the test rig is shown in Fig. 1, while for more detailed description for the experimental procedures, readers can also refer to [13].

The test rig in Fig. 1 is replicated in PowerFLOW to examine whether the pressure drop across the metal-foam could be reproduced in the simulation. The tube inlet is specified with a freestream velocity that equals the Darcian velocity (v_d), while the tube outlet is prescribed with the atmospheric pressure p_∞. The wall of the tube is given the slip boundary condition. The metal-foam sample is placed at the center of the tube, and it is represented as a 3-layer combination of APM-PM-APM. This strategy is proposed based on the following assumptions; (1) the influence of the porosity is significant only at near-surface regions (i.e., where the thickness is still comparable to the pore size [18]), and (2) the resistivity of the porous material would become independent on its thickness once the effect of porosity is negligible. These assumptions allow the APM region, which includes the porosity effects, to be specified as the outer layer of the porous material, whereas the inner layer is represented by the PM region. Furthermore, the inner PM region is provided with asymptotic resistivity values even though it might have an arbitrary shape or thickness, while the outer APM region is provided with resistivity values that correspond to its thickness. These assumptions will be verified through the simulation of the test rig, in which the APM outer layer accounts for 20 % of h (i.e., $0.1h$ thick on both ends of the sample).

4 grid refinement regions are specified in the simulation domain with the finest one covering the entire APM-PM region, such that a total of 8 voxels is used to resolve the thickness of the APM layer. It has been verified that increasing the number of voxels inside the APM-PM regions further does not affect the results.

B. Porous Trailing Edge Noise Test Case

The porous trailing edge noise test case replicates the experimental investigations of Arce-Leon et al.[32] and Rubio-Carpio et al. [10, 13]. The airfoil is a NACA 0018 with the chord length (c) of 200 mm and the span of 80 mm that is installed at zero angle of attack. This span, however, is smaller than the physical span in the experiments to reduce computational load [20, 33]. The airfoil is located inside a computational domain where the freestream velocity is $U_\infty = 20$ m/s (i.e., freestream Mach number $M_\infty = 0.06$) and the chord-based Reynolds number Re_c is 2.8×10^5. The freestream turbulence intensity is set to 0.1 %, and laminar-turbulent transition is forced on the airfoil using zig-zag strips [34] with the trip thickness of $h_{trip} = 0.6$ mm, the trip amplitude of $l_{trip} = 0.3$ mm, and the wavelength of $\lambda_{trip} = 3$ mm. The zig-zag strip is installed on both sides of the airfoil at 20 % of the chord length.
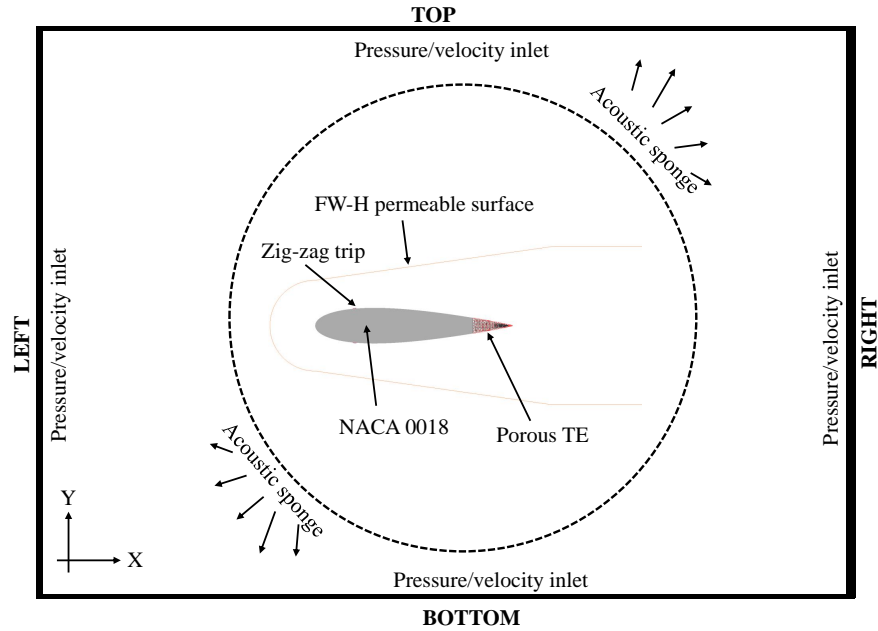
6

Fig. 2 A sketch of the computational domain for NACA 0018 trailing edge noise measurement case (not to scale).
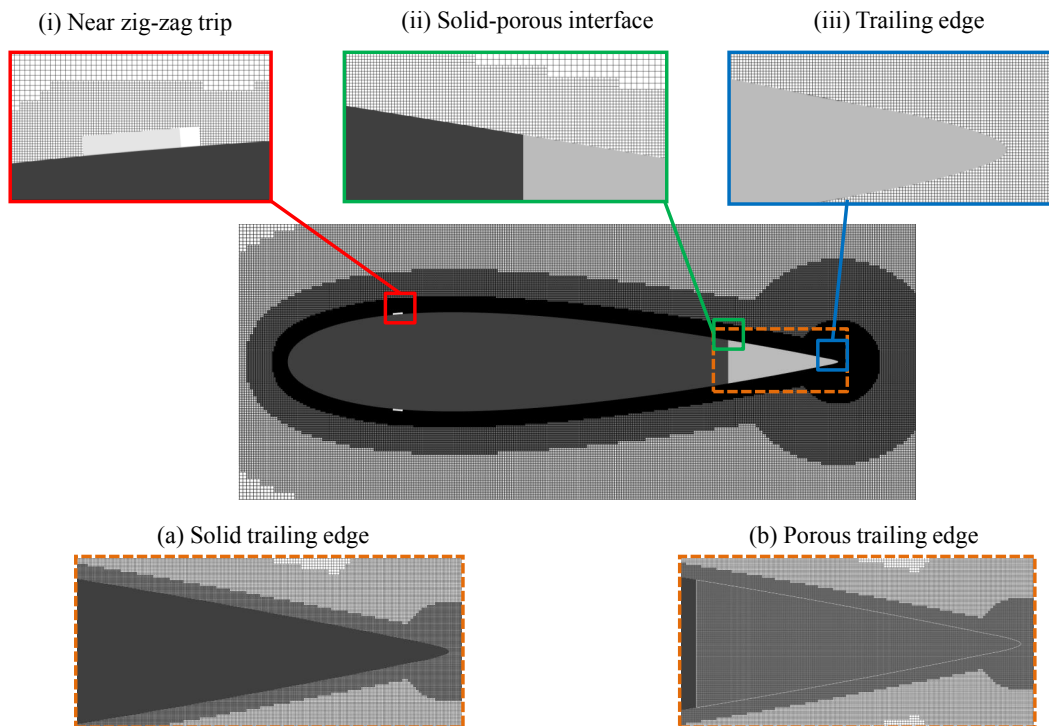

Fig. 3 The grid distribution in the simulation domain of the NACA 0018 trailing edge noise measurement case. Insets (a) and (b) show the difference of the grid configuration between the solid and porous trailing edge cases

The computational domain is shown in Fig. 2, however readers are advised that the figure is not to scale. The global coordinate system is also shown in the figure, in which X and Y axes are aligned with the freestream and its normal direction respectively. The origin of this coordinate system is at the midspan of the trailing edge (i.e., $X/c = 0$ at the trailing edge), hence the airfoil leading edge would be located at $X/c = -1$ and the airfoil spans in between $Z/c = \pm 0.2$. The computational domain is a rectangular box whose width equals the span of the airfoil, while the length and height are $100c$ long with the trailing edge of the airfoil located at the center of the domain. An acoustic sponge region is specified starting from a radius of $36c$ from the trailing edge to dampen outward traveling acoustic waves and to prevent reflection by the domain boundaries. 10 grid refinement regions are specified within the domain with the finest grid region located adjacent to the airfoil surface. The finest wall-adjacent-grid height at the trailing edge corresponds to $y^+ = 3$, which was found to produce converged results from the grid independence study. The resulting grid distribution is shown in Fig. 3. Freestream pressure and velocity is prescribed at the left, top, right, and bottom domain boundaries, as shown in Fig. 2. Periodic boundary condition is imposed on the boundaries at both ends of the airfoil. The surface of the solid parts of the airfoil and the tripping elements are no-slip walls.

The porous trailing edge is represented as a combination of APM and PM regions, where the former is a 1 mm-thick layer placed on top of the latter. Asymptotic resistivity values (i.e., the porous material resistivity above a certain critical thickness [18]), as shown in table 1, are used for the PM region, while the resistivity values corresponding to 1 mm-thick sample are applied for the APM layer. For this particular study, the properties of the metal foam with $800\,\mu m$ pore size is considered.

V. Porous Material Characterization Test Rig

The trends of the viscous resistivity R_V, the inertial resistivity R_I, and the pressure drop across the metal-foam samples are shown in Fig. 4. The resistivity values in Fig. 4 (i) were obtained from the measurements of Rubio-Carpio et al. [10] and subsequently applied to the APM and PM regions in the simulation domain. Therefore, the simulation is expected to produce pressure drop trends that are similar to those of the experiment. The Darcian velocity v_d at the inlet is specified to be $2.35\,m/s$ and $2.55\,m/s$ for $450\,\mu m$ and $800\,\mu m$ metal-foam samples respectively. In Fig. 4 (i), R_V shows more variation compared to R_I as the sample thickness decreases, similar to the observation of Dukhan and Minjeur [18]. Furthermore in Fig. 4 (ii), the APM-PM combination used in the numerical study produces good agreement against the experiment for various tested sample thickness.
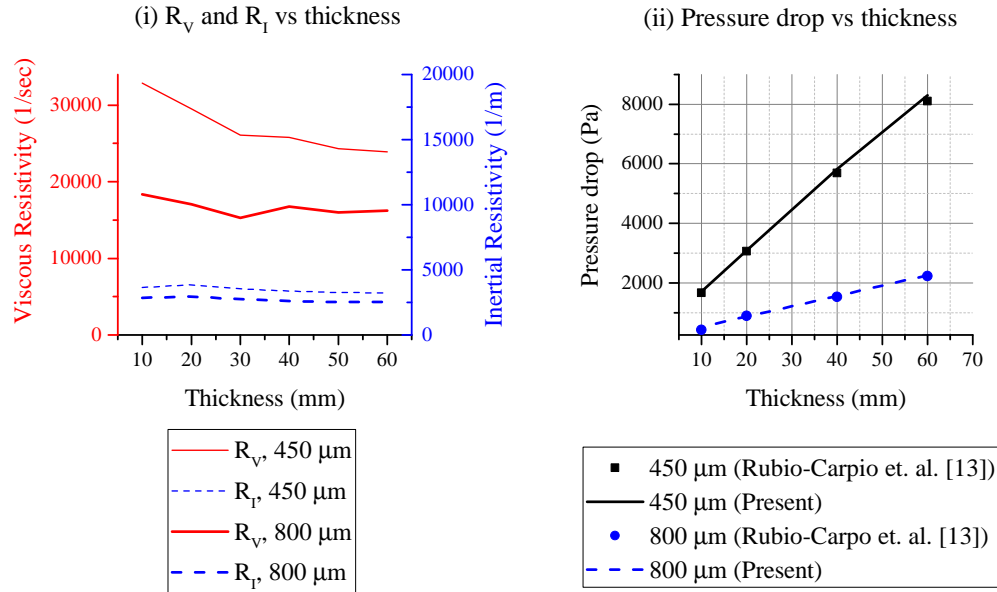

(i) R_V and R_I vs thickness

(ii) Pressure drop vs thickness

Legend (i):
— R_V, 450 µm
- - - R_I, 450 µm
— R_V, 800 µm
- - - R_I, 800 µm

Legend (ii):
■ 450 µm (Rubio-Carpio et. al. [13])
— 450 µm (Present)
● 800 µm (Rubio-Carpo et. al. [13])
- - - 800 µm (Present)

Fig. 4 Resistivity value and pressure drop variation with metal-foam sample thickness in the test rig.

The time-averaged pressure and the streamwise velocity distributions within the test rig are shown in Fig. 5. As expected, the pressure drop only takes place within the APM-PM region, and the pressure gradient in between

$-0.5 < X/h < 0.5$ is consistent regardless of the thickness or porosity (i.e., pore size). The flow velocity also increases linearly across the APM-PM region and eventually becomes constant further downstream in order to conserve the mass flux inside the tube. Overall, the trends in Fig. 5 are consistent with the single-layer-APM approach of Sun et al. [30]. This suggests that the PM-APM combination does not compromise the flow field behavior across the porous media region while allowing a more practical approach to define the properties of a porous material of an arbitrary shape.

Based on the results in this section, the APM-PM models in PowerFLOW are considered to be reliable for resolving the fluid transport phenomena across a metal-foam sample of various thickness. Nevertheless, the current application of the porous media model is focused on the metal-foam, which has isotropic and homogeneous resistivity [35]. Thus, further investigations are warranted to determine whether the APM-PM combination is also applicable for anisotropic porous materials (e.g., perforated plate).
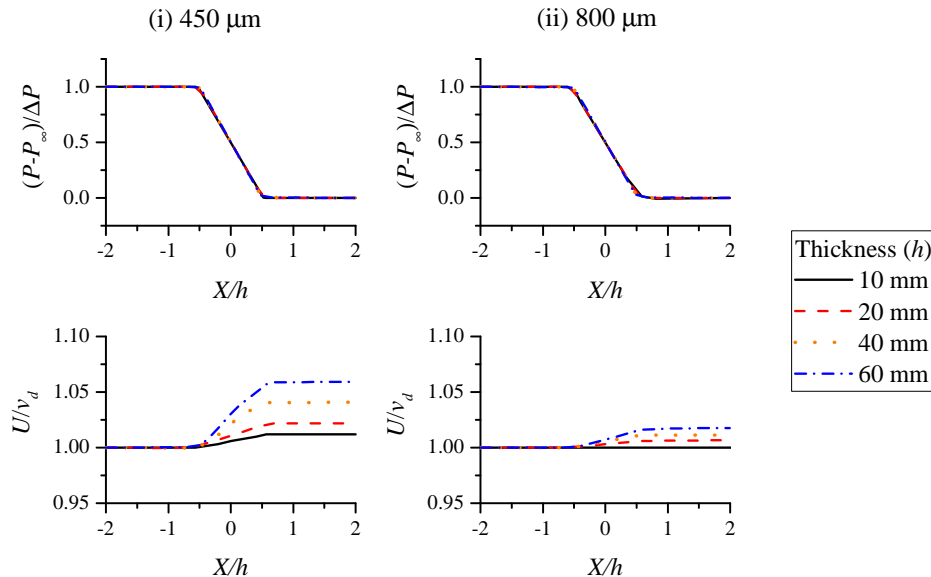
Fig. 5   Pressure and flow velocity along the centerline of the test rig.

VI. NACA 0018 with metal-foam trailing edge

A. Grid independence study

This section discusses the grid independence study for the NACA 0018 airfoil trailing edge (TE) noise case. Three grid resolution settings based on the numbers of voxels assigned along the airfoil chord are considered, and these information are summarized in Table 2. The number of voxels for the porous TE simulation is significantly higher than that of the solid TE since additional voxels of the finest resolution are added to the PM and APM regions at the trailing edge. Each case has been run for 10 flow passes after an initial transient, using a 320-core of Intel Xeon-Gold 6130 HPC facility. For reference, the finest simulation of the porous TE case requires around 9000 CPU hours per flow pass. For subsequent sections, all presented results are based on the simulation with $y^+ = 3$ unless specified otherwise.

Table 2   Simulation details for grid independence study.

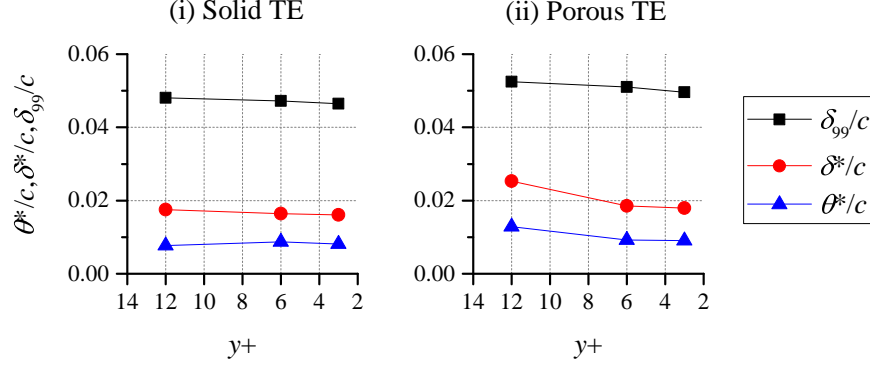| y^+	Resolution (voxels/c)	Voxel count, solid TE (10^6)	Voxel count, porous TE (10^6)
12	640	3.409	4.584
6	1280	27.28	36.67
3	2560	218.2	293.4

Fig. 6 Trend of mean boundary layer quantities versus the first wall-adjacent voxel resolution.

The effect of varying the grid resolution is assessed using the boundary layer quantities at the trailing edge ($X/c = 0$). The trends of the boundary layer thickness δ_{99}, displacement thickness δ_*, momentum thickness θ^*, and shape factor $H = \delta^*/\theta^*$ for both the solid and porous trailing edge cases are shown in Fig. 6. The trend shows all quantities tend to converge as the voxel resolution is increased. Nevertheless, the porous TE case shows larger changes compared with the solid TE one which is likely to be related with the number of voxels used to resolve the APM layer.

B. Boundary layer quantities at the trailing edge

Firstly, the flow field in the vicinity of the trailing edge is assessed to verify that boundary layer properties of the simulation are comparable to other studies. The boundary layer properties are evaluated based on the wall-parallel and wall-normal velocity components, which are defined according to the reference system shown in Fig. 7.
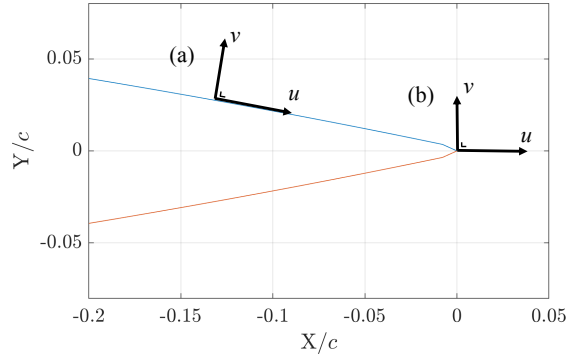
Fig. 7 Coordinate system for measuring the wall-normal (v) and wall-parallel (u) velocity components at the airfoil trailing edge (i.e., at (a) $X/c < 0$ and (b) $X/c \geq 0$). The blue line corresponds to the suction side of the airfoil and the red line to the pressure side.

Table 3 Comparison of boundary layer properties on the solid trailing edge ($X/c = 0$) against previous experimental and numerical efforts.

Solid Trailing Edge	δ_{99} (mm)	δ^* (mm)	θ^* (mm)	H
LBM-VLES, (Present)	9.31	3.37	1.61	2.09
LBM-VLES, (Avallone et al. [20])	9.50	3.30	1.50	2.20
Experiment (Rubio-Carpio et al. [13])	9.30	3.52	1.59	2.21
Experiment (Arce-Leon et al. [32])	9.40	2.10	1.30	1.62

This comparison is presented in table 3, in which the boundary layer thickness δ_{99}, displacement thickness δ^*, momentum thickness θ^*, and shape factor $H = \delta^*/\theta^*$ are reported. δ_{99} is defined as a point inside the boundary layer where the mean wall-parallel velocity equals to 99 % of the freestream velocity. Moreover, the integration limit for computing δ^* and θ^* is $0 \leq Y/c \leq 0.07$, which is the PIV volume limit of the experiment [13]. Overall, the boundary layer parameters at the trailing edge are found to be in trend against those of other studies.
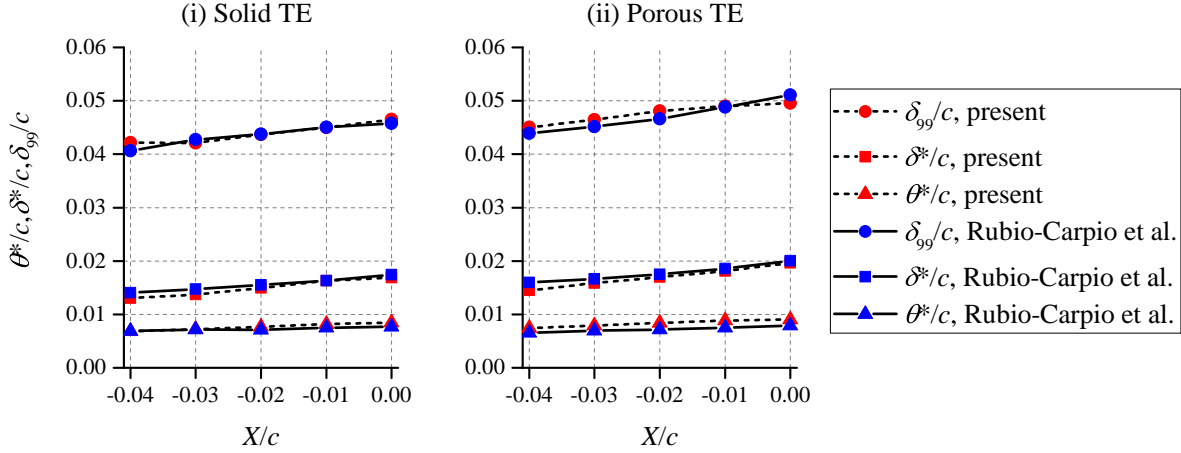
Fig. 8 Comparison of mean boundary layer quantities along the airfoil trailing edge against Ref. [13]
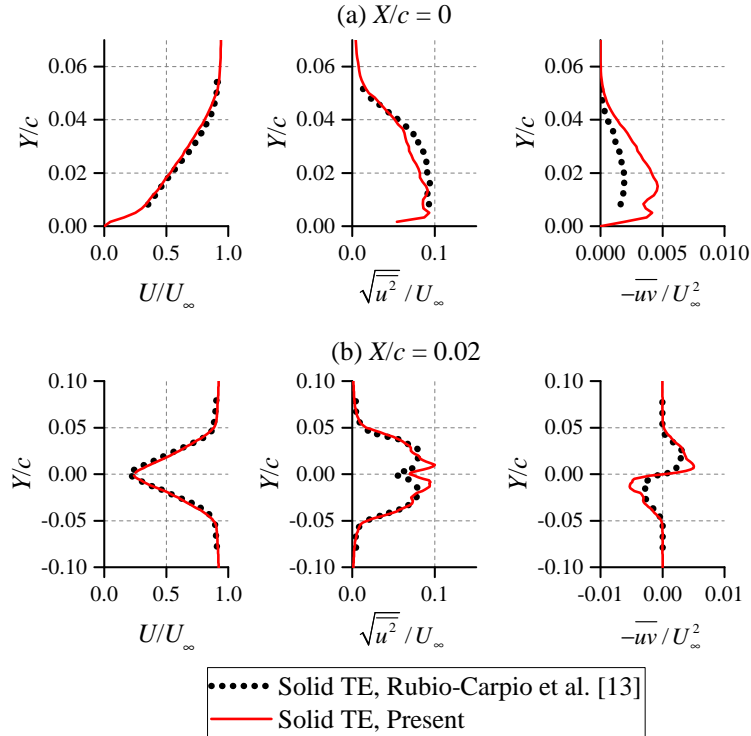
Fig. 9 Profiles of mean velocity and turbulent quantities at the trailing edge (a) and in the wake (b) for the solid TE case.
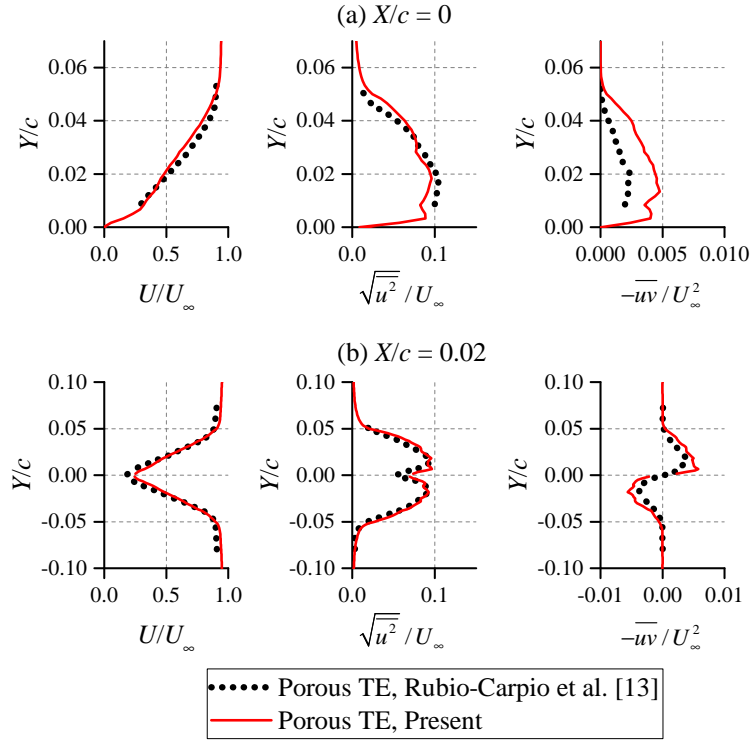
Fig. 10 **Profiles of mean velocity and turbulent quantities at the trailing edge (a) and in the wake (b) for the porous TE case.**
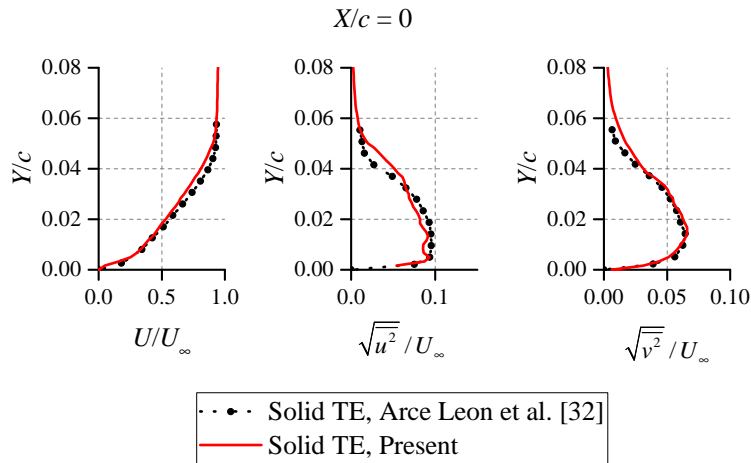
Fig. 11 **Profiles of mean velocity and turbulent quantities at the trailing edge for the solid TE case in comparison with the experiment of Arce-Leon et al.[32].**
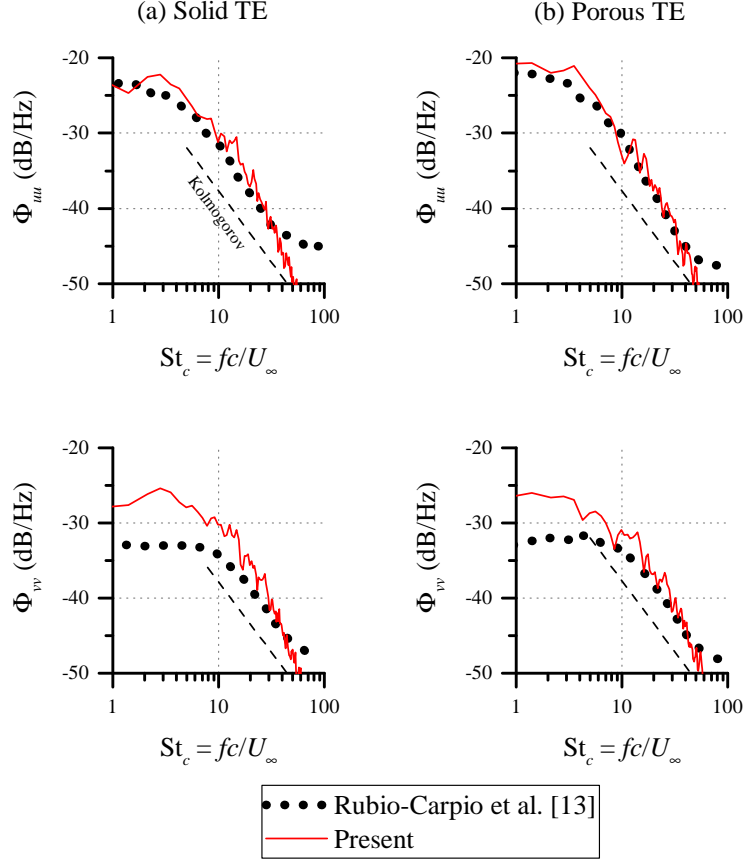
Fig. 12 **The comparison of wall-parallel (Φ_{uu}) and wall-normal (Φ_{vv}) velocity fluctuation spectra at $X/c = -0.002, Y/\delta_{99} = 0.3$.**

The comparison of the boundary layer parameters between the solid and the porous TE cases is provided in Fig. 8. In the figure, both axes are normalized with the airfoil chord. While the simulation results appear to be in good agreement with the experiment for both cases, the discrepancy is more significant in the porous TE case. It is evident that boundary layer on the porous TE is thicker than in the solid trailing edge case, which is considered to be caused by the combination of permeability [8] and the surface roughness of porous materials [13]. Since the simulation for the porous material is able to match the experimental data quite well, it is conjectured that permeability has a more significant role than the surface roughness in causing the changes in the boundary layer parameters.

The boundary layer profiles at the trailing edge ($X/c = 0$) and in the airfoil wake ($X/c = 0.02$) are shown in Fig. 9 for solid TE case and Fig. 10 for porous trailing edge case. Good agreement has been found for mean velocity quantities although there are significant discrepancies for the $-\overline{uv}$ at $X/c = 0$. As the $\sqrt{\overline{u^2}}$ component matches quite well with the experiment, the v component of the simulation might have overestimated that of the experiment. This is also evident in Fig. 12 where the velocity fluctuation spectra in the boundary layer are compared. While Φ_{uu} generally agrees well with the experiment, Φ_{vv} overestimates the experiment at lower frequency ranges up to $St_c = 10$. These discrepancies are considered to be due to the different tripping height used in the simulation (0.6 mm) and in the experiment of Rubio-Carpio et al. [13] (0.84 mm). This is also supported by the $\sqrt{\overline{v^2}}$ profile, which is in good agreement against the experiment of Arce-Leon et al. [32] (Fig. 11), where the same tripping height as in the simulation was used.

C. Flow field analyses

The mean flow-field in the vicinity of the trailing edge is depicted in Fig. 13. There is a slight difference between the trailing edge geometry in the experiment and the simulation; the latter is sharp at $X/c = 0$ while the former has a small thickness due to the limitation of manufacturing process. Nevertheless, the contours of the simulation are similar to those of the experiment. The porous trailing edge appears to have minor effect on the mean flow field, and there is

no observable steady cross-flow across the porous TE due to the lack of significant pressure difference between the opposite sides of the airfoil.

The mean surface pressure distribution in Fig. 14 (a) reveals that the porous TE has no substantial effect on the upstream pressure distribution. However, the region nearby the solid-porous interface shows an increased surface pressure, followed by an immediate reduction further downstream (see the inset in Fig. 14 (a)). The discontinuity at the solid-porous interface might have also contributed to the boundary layer thickening as shown in Fig. 15. Figure 14 (b) shows that the pressure fluctuation intensity upstream of the solid-porous interface is identical to that of the solid airfoil; the peak at $X/c = -0.7$ is caused by the tripping elements. Similar to the trend in Fig. 14 (a), the pressure fluctuation of the porous trailing edge increases immediately downstream of $X/c = -0.2$, although it gradually decreases towards $X/c = 0$.
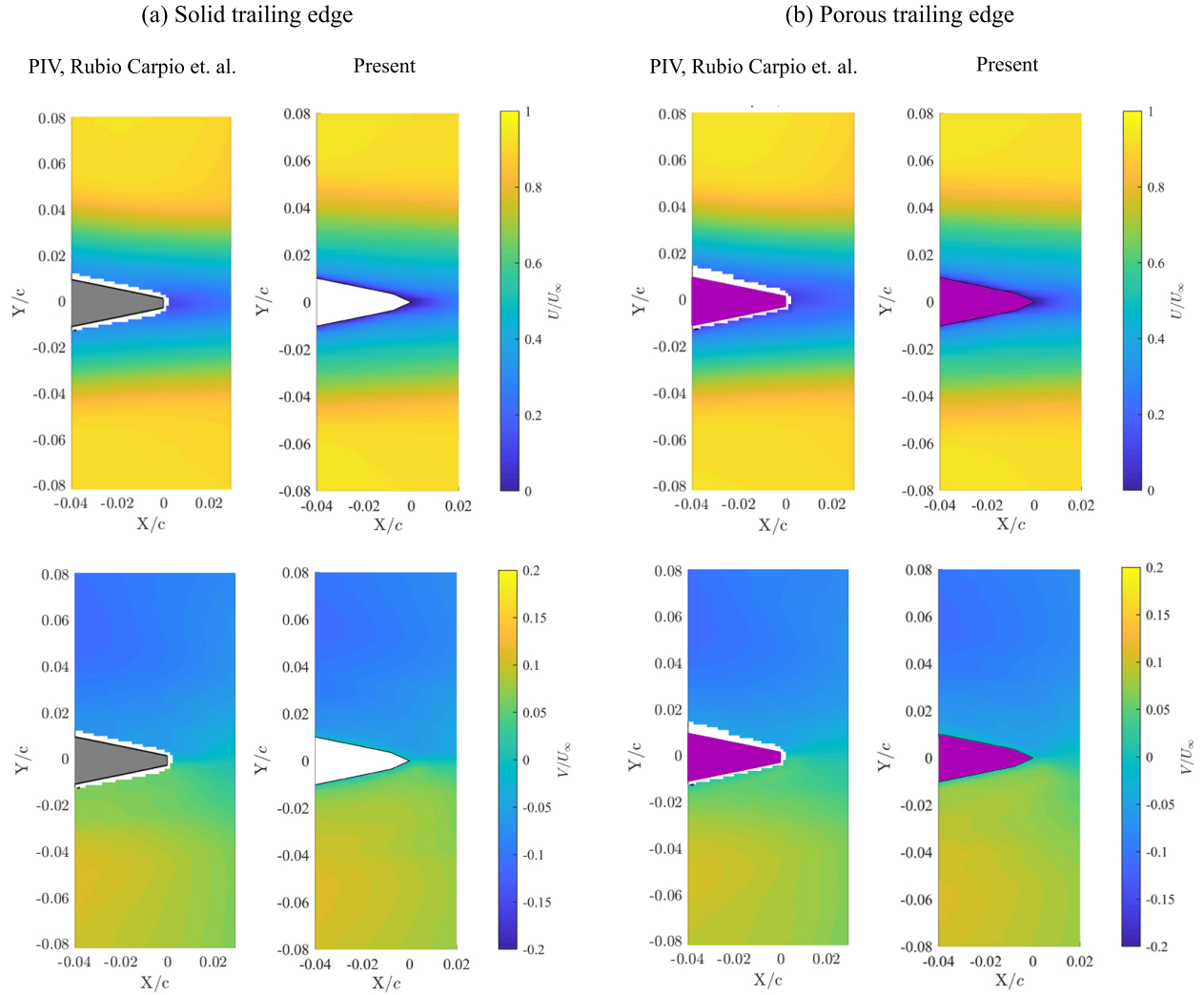
Fig. 13 **Comparison of the mean velocity components on the trailing edge against PIV measurements of Rubio Carpio et al. (some plots are reproduced from [13]).**

The spanwise correlation length of the surface pressure fluctuation $L_{pp}^Z(X)$ is also measured since it is known to be directly proportional to the TBL-TE noise intensity [4]. The spanwise correlation length distribution along the streamwise direction is shown in Fig. 16, which is defined as follows.

$$L_{pp}^Z(X) = \int_0^\infty R_{pp}^Z(X)\, d\mathbf{Z}$$
$$= \int_0^\infty \frac{\langle p'(X, \mathbf{Z} + \Delta\mathbf{Z})\, p'(X, 0)\rangle}{\langle p'(X, 0)\, p'(X, 0)\rangle}\, d\mathbf{Z} \tag{14}$$

where $R_{pp}^Z(X)$ is the correlation coefficient of surface pressure fluctuation, $\Delta\mathbf{Z}$ is the separation from a reference location $(X, 0)$ at the airfoil midspan, and $\langle \cdot \rangle$ is the ensemble-averaging operator. The correlation coefficients are computed on 12 streamwise points, where at each location, a total of 50 equidistant points with the separation of 0.2 mm are spread in the spanwise direction. The pressure fluctuation is sampled at 20 kHz for the entire simulation time. The correlation length appears to be similar for both cases at locations upstream of $X/c = -0.2$. Further downstream, the correlation length on the porous TE grows at a faster rate compared to that of the solid TE. This behavior is considered to be due to the permeability of the porous surface that would allow the influence of the flow field to extend over a longer distance. Close to $X/c = 0$, nevertheless, the correlation length on the solid trailing edge becomes comparable with that on the porous trailing edge.
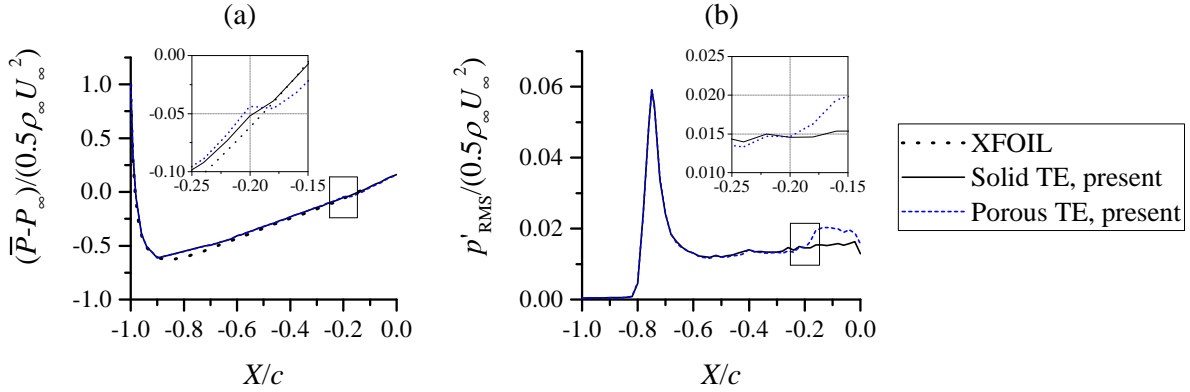

Fig. 14 **Mean surface pressure distribution (a) and the root-mean-square (RMS) of surface pressure fluctuation (b) on the NACA 0018 with solid and porous trailing edge configuration. The insets show the regions marked with the black rectangles. Discontinuity near the tripping location has been omitted.**
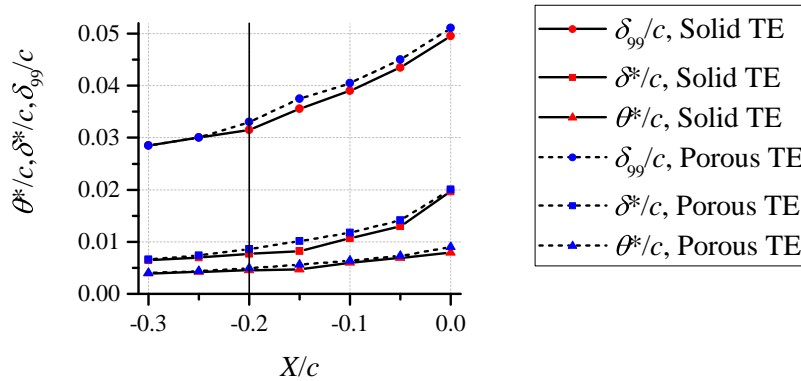

Fig. 15 **The mean boundary layer quantities comparison between the solid and porous trailing edge cases in the vicinity of the solid-porous interface. The solid line at $X/c = -0.2$ indicates the solid-porous interface location.**

Assuming that the trailing edge scattering process formulated by Amiet [3] is applicable, the airfoil with porous trailing edge is expected to produce higher noise intensity due to the stronger wall pressure fluctuation compared to its solid counterpart, and the spanwise correlation length at the trailing edge being similar for both cases. However, this is

in contrast with the experimental observations [10] and the far-field sound computations in the following section. Thus, it is reasonable to assume that a different noise generation mechanism is present in the case of porous trailing edge, which can not be considered by the classical Amiet's analytical model.
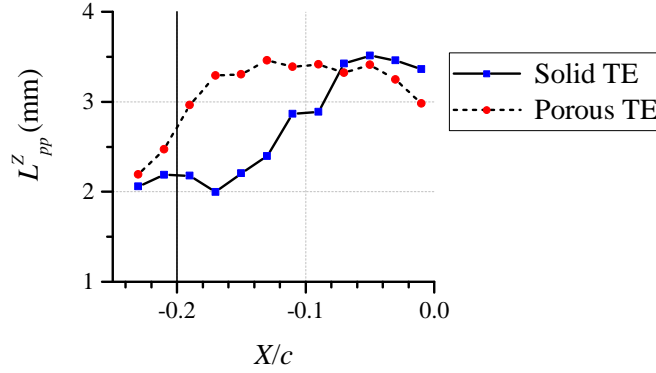

Fig. 16 **Spanwise correlation length comparison between the solid and porous trailing edge cases. The solid line at $X/c = -0.2$ indicates the solid-porous interface location.**

D. Far-field sound analyses

The far-field noise has been computed with FW-H analogy using two different sources, the surface pressure fluctuations on the airfoil and the acoustics pressure recorded by a permeable surface enclosing the airfoil. The pressure time series has been sampled for 10 flow passes over the airfoil (i.e., 0.1 s) at 120 kHz, and the resulting sound power spectra is organized into third octave bands and normalized into sound pressure level ($SPL_{1/3}$) with the reference pressure of 20 μPa. Nevertheless, to allow comparison with other references in which various airfoil span and microphone locations have been used, the sound pressure level is scaled according to Eq. 15 [20]. Meanwhile, the relative difference of the sound pressure level for both solid and porous trailing edge cases are computed as in Eq. 16.

$$SPL_{1/3,n} = SPL_{1/3} + 20\log_{10}(D) - 10\log_{10}(b) - 50\log_{10}(M_\infty) \tag{15}$$

$$\Delta SPL_{1/3,n} = SPL_{1/3,n}|_{solid} - SPL_{1/3,n}|_{porous} \tag{16}$$

The far-field sound spectra comparison between the solid and porous airfoils are shown in Fig. 17. For solid airfoil, both surface and permeable FW-H results are similar, although there are discrepancies for up to 4 dB above $St_c > 12$ for the porous airfoil case. This discrepancy indicates that there might be additional high-frequency sources that are generated inside the porous media region whose contribution would be excluded when surface FW-H formulation is used.

The spectra for the solid airfoil shows similar trend when compared to the experiment of Rubio-Carpio et al.[13] and Arce-Leon et al. [32], although the agreement with the latter is better. This might be related with the wall-normal velocity fluctuation trend (i.e., Fig. 10 and 11). Similarly, the spectra for the porous trailing edge case are also in good agreement with the experiment up to $St_c = 12$, and as expected, there is no noise increase in the high frequency, unlike in the experiment. This further suggests that the high frequency noise produced by the porous trailing edge is dominated by the contribution of the surface roughness noise.

Conventional beamforming technique [36] has been used to allow sound sources on the airfoil surface to be localized. For this purpose, FW-H analogy is also used to compute far-field sound at the locations of an array of microphones. The array arrangement is the same as the one mounted in the V-Tunnel of TU Delft [37], which has also been used for the experiment of Rubio-Carpio et al. [13]. The frontal view of the beamforming array is shown in Fig. 18. The array is a modified version of Underbrink's multi-arm spiral design [38] with an effective diameter of 2 m in the streamwise direction and 1 m in the spanwise direction. The geometrical center of the array is aligned with midspan of the airfoil trailing edge. The distance between the array plane and the scan plane on the airfoil is 1.48 m.
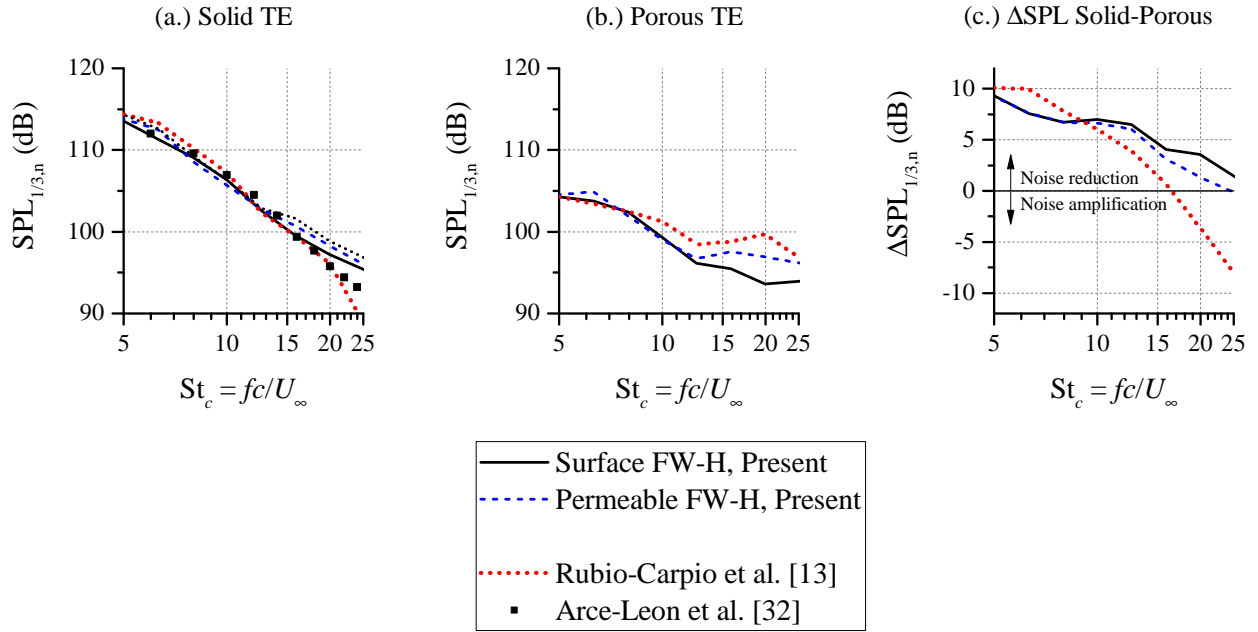
Fig. 17 **Far-field sound pressure level in third-octave bands** (SPL$_{1/3,n}$) **for the NACA 0018 with solid trailing edge (a) and porous trailing edge (b), as well as the** SPL$_{1/3,n}$ **difference (c).**
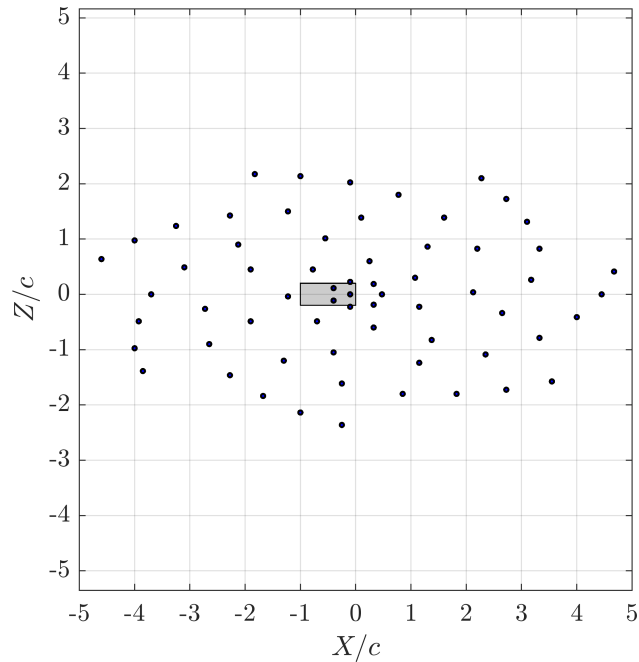

Fig. 18 **The modified Underbrink's array that is used in present study. The airfoil position is indicated as the area in grey.**

The beamforming results are shown in Fig. 19, in which the maps are plotted for 3 third-octave bands. Notice that the colormap scale for Fig. 19 (i) is different between both airfoil cases in order to emphasize the dominant source location. The contours at the higher frequency ranges, i.e., Fig. 19 (iii) appear to be smeared towards the upstream direction, which might be due to the self-noise of the tripping elements. Nevertheless, the beamforming array would not be able to distinguish the sources on the tripping elements since the Rayleigh limit at that particular frequency (i.e.,

17

2000 Hz) is estimated to be around 165 mm which is longer than the distance between the zig-zag trip and the trailing edge.

(i) 1250 Hz   (ii) 1600 Hz   (iii) 2000 Hz

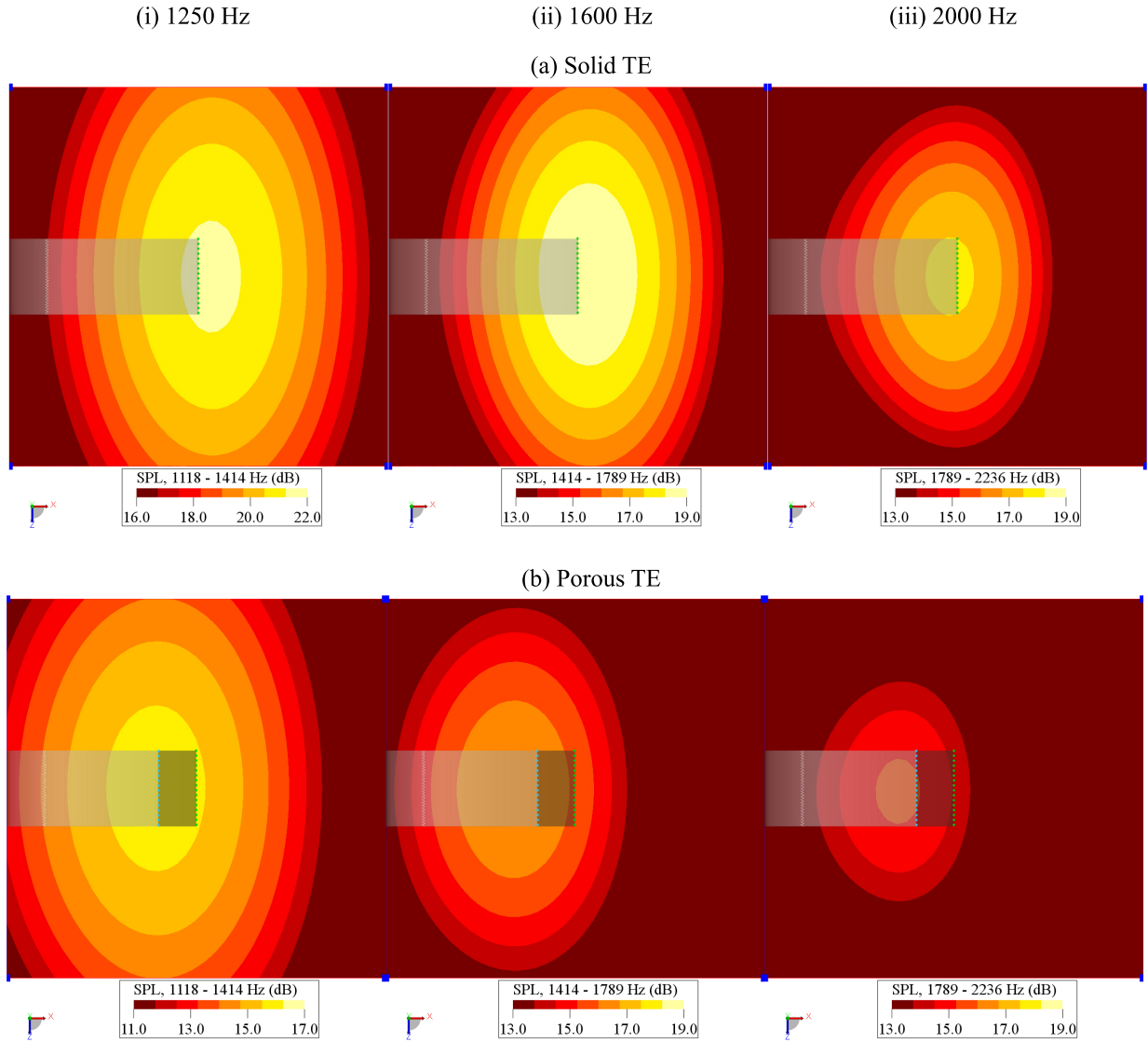(a) Solid TE

(b) Porous TE

Fig. 19   Source maps comparison between the solid (a) and porous (b) trailing edge cases for third octave bands that correspond to the central frequency of (i) 1250 Hz, (ii) 1600 Hz, (iii) 2000 Hz. The porous trailing edge is colored in dark grey. The trailing edge is indicated as green dotted line, while the solid-porous interface with blue dotted line.

The peak of the source map of the airfoil with the porous trailing edge is located next to the solid-porous interface (i.e., dotted blue line), while in the case of the solid airfoil, the peak is lined up with the trailing edge (i.e., dotted green line). This behavior has also been reported in the experiment [13], and the reason for this is considered to be the additional acoustic scattering due to sudden surface impedance jump as the boundary layer travels over the solid-porous interface [10, 39]. This observation also corroborated the idea that the noise generation mechanism of the airfoil with the porous trailing edge is indeed different compared to that of the solid trailing edge. Further analyses using the simulation results are warranted to gain better insights on the noise mitigation mechanism of the porous trailing edge.

VII. Conclusion and Outlook

This manuscript has presented a numerical study on the application of porous material to reduce trailing edge noise. The porous material was replicated in a lattice-Boltzmann solver using the porous media (PM) and acoustic porous media (APM) models based on the Darcy's law. The models characterized the porous material using the porosity, permeability (i.e., viscous resistivity) and form coefficient (i.e., inertial resistivity). Additionally, the APM considered the porosity of the material to account for the fluid interaction at the surface of the porous material. Empirical parameters were used for both the PM and the APM models. The PM-APM combination was verified using the case of a porous material characterization rig. Pressure drop trends across the porous media were compared with those from prior experiments [10, 13] and good agreement was observed. Furthermore, the pressure and velocity distributions along the test rig remained consistent for a wide variation of the tested sample thickness.

The PM-APM combination was subsequently used to emulate the metal-foam trailing edge of a NACA 0018 airfoil at zero angle of attack. Integral boundary layer parameters were measured and found to be in good agreement against those of the experiment. Far-field sound was computed using acoustics analogy and the results were generally matching the experimental data, although the noise increase at high frequency was not reproduced. The lower noise produced by the porous trailing edge was also found to be contradictory with the trend suggested in Amiet's model, since the pressure fluctuation intensity on the porous trailing edge was higher than its solid counterpart, while the spanwise correlation length at the trailing edge was similar. It is conjectured that the porous trailing edge might have a different noise generation mechanism. Moreover, the beamforming technique revealed that the solid-porous interface, instead of the actual trailing edge, was the dominant source for the porous trailing edge case. Further analyses into these aspects using the simulation results would bring better understanding on the underlying noise reduction mechanism of the metal-foam trailing edge.

Acknowledgments

References

[1] Revell, J., Revell, J., Kuntz, H., Balena, F., Horne, C., Storms, B., Dougherty, R., Kuntz, H., Balena, F., Horne, C., et al., "Trailing-edge flap noise reduction by porous acoustic treatment," *3rd AIAA/CEAS aeroacoustics conference*, 1997, p. 1646.

[2] Oerlemans, S., Fisher, M., Maeder, T., and Kögler, K., "Reduction of wind turbine noise using optimized airfoils and trailing-edge serrations," *AIAA journal*, Vol. 47, No. 6, 2009, pp. 1470–1481.

[3] Amiet, R. K., "Noise due to turbulent flow past a trailing edge," *Journal of sound and vibration*, Vol. 47, No. 3, 1976, pp. 387–393.

[4] Howe, M. S., "A review of the theory of trailing edge noise," *Journal of sound and vibration*, Vol. 61, No. 3, 1978, pp. 437–465.

[5] Gruber, M., Joseph, P., and Chong, T. P., "Experimental investigation of airfoil self noise and turbulent wake reduction by the use of trailing edge serrations," *16th AIAA/CEAS aeroacoustics conference*, 2010, p. 3803.

[6] Chong, T. P., Vathylakis, A., Joseph, P. F., and Gruber, M., "Self-noise produced by an airfoil with nonflat plate trailing-edge serrations," *AIAA journal*, Vol. 51, No. 11, 2013, pp. 2665–2677.

[7] Herr, M., and Dobrzynski, W., "Experimental Investigations in Low-Noise Trailing Edge Design." *AIAA journal*, Vol. 43, No. 6, 2005, pp. 1167–1175.

[8] Geyer, T., Sarradj, E., and Fritzsche, C., "Measurement of the noise generation at the trailing edge of porous airfoils," *Experiments in Fluids*, Vol. 48, No. 2, 2010, pp. 291–308.

[9] Geyer, T. F., and Sarradj, E., "Trailing edge noise of partially porous airfoils," *20th AIAA/CEAS Aeroacoustics Conference*, 2014, p. 3039.

[10] Rubio Carpio, A., Merino Martinez, R., Avallone, F., Ragni, D., Snellen, M., and van der Zwaag, S., "Broadband Trailing-Edge Noise Reduction Using Permeable Metal Foams," *INTER-NOISE and NOISE-CON Congress and Conference Proceedings*, Vol. 255, Institute of Noise Control Engineering, 2017, pp. 2755–2765.

[11] Sarradj, E., and Geyer, T., "Noise generation by porous airfoils," *13th AIAA/CEAS Aeroacoustics Conference (28th AIAA Aeroacoustics Conference)*, 2007, p. 3719.

[12] Geyer, T., Sarradj, E., and Fritzsche, C., "Porous airfoils: noise reduction and boundary layer effects," *International journal of aeroacoustics*, Vol. 9, No. 6, 2010, pp. 787–820.

[13] Rubio Carpio, A., Avallone, F., and Ragni, D., "On the Role of the Flow Permeability of Metal Foams on Trailing Edge Noise Reduction," *2018 AIAA/CEAS Aeroacoustics Conference*, 2018, p. 2964.

[14] Liu, H., Wei, J., and Qu, Z., "The interaction of porous material coating with the near wake of bluff body," *Journal of Fluids Engineering*, Vol. 136, No. 2, 2014, p. 021302.

[15] Liu, H., Azarpeyvand, M., Wei, J., and Qu, Z., "Tandem cylinder aerodynamic sound control using porous coating," *Journal of Sound and Vibration*, Vol. 334, 2015, pp. 190–201.

[16] Ingham, D. B., and Pop, I., *Transport phenomena in porous media*, Elsevier, 1998.

[17] Freed, D. M., "Lattice-Boltzmann method for macroscopic porous media modeling," *International Journal of Modern Physics C*, Vol. 9, No. 08, 1998, pp. 1491–1503.

[18] Dukhan, N., and Minjeur, C., "Minimum Thickness for Open-Cell Metal Foam to Behave as a Porous Medium," *40th Fluid Dynamics Conference and Exhibit*, 2010, p. 4618.

[19] Succi, S., *The Lattice Boltzmann Equation: for Fluid Dynamics and Beyond*, Oxford university press, 2001.

[20] Avallone, F., van der Velden, W., Ragni, D., and Casalino, D., "Noise reduction mechanisms of sawtooth and combed-sawtooth trailing-edge serrations," *Journal of Fluid Mechanics*, Vol. 848, 2018, pp. 560–591.

[21] Teruna, C., Casalino, D., Ragni, D., and Avallone, F., "Numerical Analysis of a Linear Cascade Model for Rotor-Stator Interaction Aeroacoustics," *2018 AIAA/CEAS Aeroacoustics Conference*, 2018, p. 4189.

[22] Chen, H., Chen, S., and Matthaeus, W. H., "Recovery of the Navier-Stokes equations using a lattice-gas Boltzmann method," *Physical Review A*, Vol. 45, No. 8, 1992, p. R5339.

[23] Bhatnagar, P. L., Gross, E. P., and Krook, M., "A model for collision processes in gases. I. Small amplitude processes in charged and neutral one-component systems," *Physical review*, Vol. 94, No. 3, 1954, p. 511.

[24] Yakhot, V., and Orszag, S. A., "Renormalization group analysis of turbulence. I. Basic theory," *Journal of scientific computing*, Vol. 1, No. 1, 1986, pp. 3–51.

[25] Launder, B. E., and Spalding, D. B., "The numerical computation of turbulent flows," *Numerical Prediction of Flow, Heat Transfer, Turbulence and Combustion*, Elsevier, 1983, pp. 96–116.

[26] Williams, J. F., and Hawkings, D. L., "Sound generation by turbulence and surfaces in arbitrary motion," *Phil. Trans. R. Soc. Lond. A*, Vol. 264, No. 1151, 1969, pp. 321–342.

[27] Farassat, F., and Succi, G. P., "A review of propeller discrete frequency noise prediction technology with emphasis on two current methods for time domain calculations," *Journal of Sound and Vibration*, Vol. 71, No. 3, 1980, pp. 399–419.

[28] Casalino, D., "An advanced time approach for acoustic analogy predictions," *Journal of Sound and Vibration*, Vol. 261, No. 4, 2003, pp. 583–612.

[29] Li, X., Li, X., and Tam, C., "Construction and validation of a broadband time domain impedance boundary condition," *17th AIAA/CEAS Aeroacoustics Conference (32nd AIAA Aeroacoustics Conference)*, 2011, p. 2870.

[30] Sun, C., Pérot, F., Zhang, R., Lew, P.-T., Mann, A., Gupta, V., Freed, D. M., Staroselsky, I., and Chen, H., "Lattice Boltzmann formulation for flows with acoustic porous media," *Comptes Rendus Mécanique*, Vol. 343, No. 10-11, 2015, pp. 533–544.

[31] Perot, F., and Freed, D., "Acoustic absorption of porous materials using LBM," *19th AIAA/CEAS Aeroacoustics Conference*, 2013, p. 2070.

[32] León, C. A., Merino-Martínez, R., Ragni, D., Avallone, F., and Snellen, M., "Boundary layer characterization and acoustic measurements of flow-aligned trailing edge serrations," *Experiments in Fluids*, Vol. 57, No. 12, 2016, p. 182.

[33] Romani, G., van der Velden, W. C., and Casalino, D., "Deterministic and statistical analysis of trailing-edge noise mechanisms with and without serrations," *2018 AIAA/CEAS Aeroacoustics Conference*, 2018, p. 3129.

[34] van der Velden, W., van Zuijlen, A., de Jong, A., and Ragni, D., "Flow and self-noise around bypass transition strips," *Noise Control Engineering Journal*, Vol. 65, No. 5, 2017, pp. 434–445.

[35] Yang, X., Lu, T. J., and Kim, T., "An analytical model for permeability of isotropic porous media," *Physics Letters A*, Vol. 378, No. 30-31, 2014, pp. 2308–2311.

[36] Mueller, T. J., and Lynch, D. A., "An anechoic facility for basic aeroacoustic research," *Aeroacoustic Measurements*, Springer, 2002, pp. 258–308.

[37] Luesutthiviboon, S., Malgoezar, A., Snellen, M., Sijtsma, P., and Simons, D., "Improving source discrimination performance by using an optimized acoustic array and adaptive high-resolution CLEAN-SC beamforming," *7th Berlin Beamforming Conference*, 2018, pp. 1–27.

[38] Underbrink, J. R., "Circularly symmetric, zero redundancy, planar array having broad frequency range applications," , Mar. 20 2001. US Patent 6,205,224.

[39] Kisil, A., and Ayton, L. J., "Aerodynamic noise from rigid trailing edges with finite porous extensions," *Journal of Fluid Mechanics*, Vol. 836, 2018, pp. 117–144.